Detectable regional changes in the number of warm nights

S. Morak,[1] G. C. Hegerl,[1] and J. Kenyon[2]

Received 14 June 2011; revised 9 August 2011; accepted 10 August 2011; published 8 September 2011.

[1] In this study we analyse gridded observed and multi-model simulated trends in the annual number of warm nights during the second half of the 20th century. We show that there is evidence that external forcing has significantly increased the number of warm nights, both globally and over many regions. We define thirteen regions with a high density of observational data over two datasets, for which we compare observed and simulated trends from 20th century simulations. The main analysis period is 1951–1999, with a sub-period of 1970–1999. In order to investigate if observed trends changed past 1999, we also analysed periods of 1955–2003 and 1974–2003. Both observed and ensemble mean model data from all models analysed show a positive trend for the regional mean number of warm nights in all regions within this 49 year period (1951–1999). The trends tend to become more pronounced over the sub-period 1970–1999 and even more so up to 2003. We apply a fingerprint analysis to assess if trends are detectable relative to internal climate variability. We find that changes in the global scale analysis, and in 9 out of 13 regions, are detectable at the 5% significance level. A large part of the observed global-scale trend in TN90 results from the trend in mean temperature, which has been attributed largely to anthropogenic greenhouse gas increase. This suggests that the detected global-scale trends in the number of warm nights are at least partly anthropogenic. **Citation:** Morak, S., G. C. Hegerl, and J. Kenyon (2011), Detectable regional changes in the number of warm nights, *Geophys. Res. Lett.*, *38*, L17703, doi:10.1029/2011GL048531.

1. Introduction

[2] Station data extending over more than a hundred years show a strong increase in temperature over the last 50–100 years, which affects both mean and extreme temperature. Changes in temperature extremes have been documented and analysed with the guidance of the expert team on climate change detection and indices (ETCCDI) [*Karl et al.*, 1999; *Alexander et al.*, 2006].

[3] Understanding, attributing and predicting changes in the probability of extremes is of great importance, as extreme events can have a strong influence on society and ecosystems. For example, extremely hot nights can seriously affect human health during heat waves [*Karl et al.*, 2008].

[4] *Alexander et al.* [2006] and the work by *Tebaldi et al.* [2006] [see also *Karl et al.*, 2008] show increases in temperature extremes, in particular a significant increase in the number of warm minimum temperatures and a generally smaller increase in the number of warm maximum temperatures. A decrease in the cold tails of both minimum and maximum temperature [*Alexander et al.*, 2006; *Karl et al.*, 2008; *Tebaldi et al.*, 2006] and a decrease in the daily temperature range (DTR) has been observed during the second half of the 20th century [*Vose et al.*, 2005], the latter of which has flattened in the last two decades [*Trenberth et al.*, 2007]. Furthermore, widespread increases in heat waves and decreases in frost days have also been recorded [*Tebaldi et al.*, 2006].

[5] The changes in extremes described above show distinct geographical patterns. For instance, a strong reduction in frost days accompanied by an increase in season length are found in the north western region of the US and Eastern Europe, while South Western North America shows a development towards higher numbers of heat waves [*Tebaldi et al.*, 2006]. In contrast, increases in the number of hot extremes across Eastern North America are modest, with decreases in parts of the South Eastern North America region [*Portmann et al.*, 2009]. Besides external influences, global circulation patterns can also influence the number and intensity of temperature extremes [*Kenyon and Hegerl*, 2007; *Scaife et al.*, 2008].

[6] Detection and attribution is used to identify if a detectable climate change signal is caused by external forcing, for example anthropogenic influences. This method compares an observed change in climate to the expected change in response to changes in external forcing. A significant change in climate is detected if the likelihood of the occurrence of this change solely due to internal variability is small. *Stott* [2003] and *Stott et al.* [2010] show, using optimal fingerprints, that changes in global and regional surface temperatures can be detected and largely attributed to greenhouse gas increases [see also *Hegerl et al.*, 2007]. *Christidis et al.* [2005] show that the pattern of change in the warmest night, and the coldest day and night during the second half of the 20th century can be detected, and attributed at least in part to anthropogenic forcing, while no change could be detected in the warmest day.

2. Data and Pre-processing

[7] This study is based on a comparison of observed and modeled annual data of the index TN90. This index is defined as the mean number of warm nights with a minimum temperature exceeding the 90th percentile of the daily minimum temperatures of the climatological period 1961–1990 at a given location and over one year. We used five different coupled climate models, each of which consist of three individual runs, giving 15 model simulations and compare these to two observational datasets. For our analysis we selected eleven out of 32 regions introduced by Giorgi [*Giorgi and Francisco*, 2000], whose data coverage for TN90 is deemed sufficient to provide a credible regional average (see Table 1, regions 1–11). We also analyse two smaller subregions, one in the South East of North America (SENA) and one in

[1]School of Geosciences, University of Edinburgh, Edinburgh, UK.
[2]Nicholas School of the Environment and Earth Sciences, Duke University, Durham, North Carolina, USA.

0094-8276/11/2011GL048531

Table 1. Table of Regions[a]

Number	Acronym	Name of Region	Latitude (°N)	Longitude (°E)	*Corr* (T_{mean})	$\frac{Trend_{T_{mean}}}{Trend_{TN90}}$ (%)
0	GLOB	Global Mean	−85/85	−175/180	0.8804	**72%**
1	SAU	Southern Australia	−45/−30	110/155	0.8254	**71%**
2	ALA	Alaska	60/85	−170/−105	0.8858	**91%**
3	WNA	Western North America	30/60	−130/−105	0.7890	45%
4	CNA	Central North America	30/50	−105/−85	0.7909	18%
5	ENA	Eastern North America	25/50	−85/−60	0.8038	13%
6	NEU	Norther Europe	45/75	−10/40	0.8630	**60%**
7	MED	Mediterranean	30/45	−10/40	0.7599	**53%**
8	NAS	Northern Asia	50/70	40/180	0.8814	**64%**
9	WAS	Western Asia	30/50	40/75	0.8419	**58%**
10	TIB	Tibet	30/50	75/100	0.7338	19%
11	EAS	Eastern Asia	20/50	100/145	0.8839	**90%**
12	SENA	South-East North America	30/40	−100/−75	0.7717	1%
13	CEU	Central Europe	45/50	0/20	0.7999	**75%**

[a]Columns 1–3 show the number of the region, its acronym and its name. Columns 4 and 5 list the latitudinal and longitudinal span of each region. Column 6 shows the correlation coefficient of inter-annual variation (trend subtracted) in observed TN90 with the observed annual mean T_{mean}. Column 7 explains how much of the observed trend in TN90 can be explained by the observed trend in T_{mean}. Bold numbers highlight the regions where at least 50% of the observed trend in TN90 can be explained by T_{mean}.

Central Europe (CEU), for a more detailed description of these two regions of interest see Table 1 (regions 12 and 13).

2.1. Observational Data Sets

[8] The two observational datasets are based on similar input stations [*Kenyon and Hegerl*, 2007; *Alexander et al.*, 2006] but on different processing techniques to arrive at gridded data for TN90. Thus, they provide a first estimate of the role of processing uncertainty:

[9] 1. The "Duke Data Set," covering 1886–2005, with a grid resolution 5° × 5° was produced by binning values of the TN90 index into grid boxes and then averaging to provide a grid box value. The station data are the same as used by *Kenyon and Hegerl* [2007]. The ETCCDI station data were provided from Lisa Alexander [*Alexander et al.*, 2006]. The gridded values are based on a varying number of observations per grid and thus can be noisy if there is just a single or a few point measurements representing the value of an entire grid box. Furthermore there are quite a lot of unobserved regions in this data set, as grid boxes without stations remain blank.

[10] 2. The HadEX data set (grid resolution 3.75° × 2.5°) was produced by the Hadley Centre [*Alexander et al.*, 2006], by applying a spatial interpolation scheme to the ETCCDI index data. The HadEX data set shows a higher spatial coverage than the gridded station-based data set, but interpolates further between stations. This makes the data set much more spatially uniform, but also less anchored in close-by station data. The data set covers the years 1950–2003.

[11] For analysing causes of the observed change, we also used monthly mean daily minimum, mean and maximum surface temperature data from the Climatic Research Unit (CRU) [*Brohan et al.*, 2006].

2.2. Modeled Data Sets

[12] The model simulated data sets were calculated from daily data from CMIP3 climate model simulations by Julie Arblaster and Claudia Tebaldi [*Tebaldi et al.*, 2006]. We picked five models (listed below) that offered at least three single runs. We use three runs each in order to give equal weight to each of the models in the multi-model mean. The data cover the years 1951–1999 and have been linearly interpolated to a grid resolution of 2.5° × 2.5° by Tebaldi and Arblaster [*Tebaldi et al.*, 2006]. All climate model simulations were forced with estimates of observed forcing over the 20th century, including changing concentrations of greenhouse gases, tropospheric and stratospheric aerosols, changes in solar radiation and volcanoes, although forcing details and implementation vary between models. We use data of the following OAGCMs.

[13] 1. GFDL-CM2.0 has an atmospheric resolution of the 2° × 2.5° and L24. The oceanic resolution is 0.3° − 1.0° × 1.0°.

[14] 2. GFDL-CM2.1 has the same resolution as GFDL-CM2.0 but the atmospheric circulation is based on semi-Lagrangian transports.

[15] 3. MIROC3.2 (hires) has an atmospheric resolution of T106 (~1.1° × 1.1°) and L56. The resolution of the ocean is 0.2° × 0.3° and L47.

[16] 4. MRI-CGCM2.3.2 has a atmospheric resolution of T42 (~2.8° × 2.8°) and L30, with its top at 0.4 hPa. The oceanic resolution is 0.5° − 2.0° × 2.5° and L23.

[17] 5. PCM1 has an atmospheric resolution of T42 (~2.8° × 2.8°) and L26. Its oceanic resolution is 0.5° − 0.7° × 1.1° and L40.

[18] For comparison with the Duke gridded indices, the model data and the HadEX data are re-gridded to a resolution of 5° × 5° per grid box by linear 2D interpolation. Furthermore, the model data and the HadEX data are masked in space and time to reflect the sampling of the Duke data (referred to as "MASK DUKE"). The longest period that is covered by both observed and model simulated data is 1951–1999. Having 49 years of data, we first calculate the decadal trend for each 5° × 5° grid box by fitting a slope-line with a least square fit (Figure 1a). Linear trends are only fitted to grid-boxes where at least five years are available during the first and last decade of the trend period. In order to reduce the noise of the spatial trend pattern we apply a 5-point smoother to all trend patterns, by averaging each grid-box with its nearest neighbours, or a subset thereof, based on availability. After computing the trend values and after the smoothing we determine the spatial average of the trend for all 13 regions as well as the global-scale trend by averaging over 11 out of 13 regions (see Figures 2a and 2b). The South-Eastern North American region (SENA) and the Central European region (CEU) are

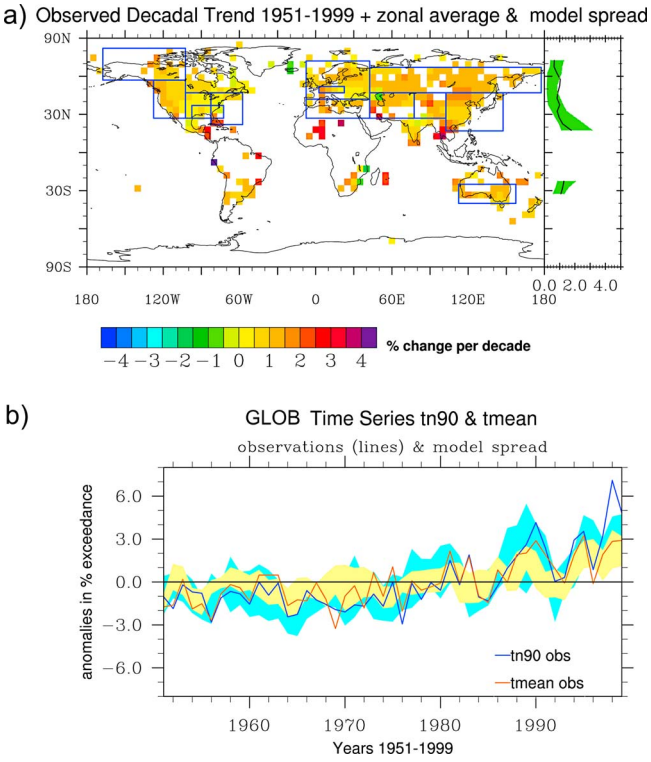

Figure 1. (a) 1951–1999 observed decadal trend of TN90 (in % change per decade) derived from the Duke data set. The zonal average of the observations (black line) and the model spread (green shaded area), is shown on the side of the plot. (b) Global mean time series of observed TN90 (blue line) and regressed time series of observed Tmean (orange line) onto TN90. Shading shows the model spread of TN90 in blue and the regressed model spread of Tmean on TN90 for individual simulations in yellow.

excluded from averaging as they overlap with other larger regions.

3. Methods

[19] We determined if the observed trend could be explained by the fingerprint of externally driven changes plus variability. The fingerprint is derived from the average of all climate model simulations used, while the deviation from the ensemble mean, which is distinct for each ensemble member, is used to estimate variability. For the fingerprint analysis we calculate how the spatial pattern of trends from the multi model mean (fingerprint f) needs to be scaled to best match the observed trends y. This is done for individual regions as well as for a global pattern of regional mean trends. The scaling factors (α) are estimated using least squares regression (we do not use an "optimal" fingerprinting method, see *Hegerl et al.* [2007] and *Allen and Tett* [1999] for a description of fingerprint methods):

$$y = \alpha f + res \tag{1}$$

$$\alpha = \frac{f^T y}{f^T f} \tag{2}$$

f denotes the fingerprint vector ($f_1 \ldots f_j$), where f_i is the decadal trend value of TN90 of the multi-model mean for one grid box, $y(y_1 \ldots y_j)$ represents the decadal trend value of TN90 of the observations (either Duke or HadEX) or of the samples of variability (see below), where y_i is the decadal trend value of TN90 for one grid box. To determine the uncertainty range of this scaling factor we estimated scaling factors from samples of trend patterns associated with internal climate variability.

[20] These samples for uncertainty due to internal climate variability ($i = 1,\ldots,j$) are estimated from the model simulated variability of each individual model $model_i$, around the mean change ($\overline{model}$) using

$$uncertainty_i = \left[model_i - \overline{model}\right] * correction \tag{3}$$

The model uncertainty $uncertainty_i$ covers the model error combined with the internal variability. By applying the fingerprint analysis to all available values of "$uncertainty_i$", we get an estimate of the internal variability. The correction against bias due to subtraction of the mean is given by:

$$correction = \sqrt{\frac{n}{n-1}}, \tag{4}$$

with n being the number of individual simulations, 15 in this case. The uncertainty in α is estimated by calculating the 5–95% range of scaling factors arising from these individual noise samples, using a t-test with 14 degrees of freedom [see *von Storch and Zwiers*, 2000]. If the scaling factor α, estimated from the observations, is significantly larger than explained by noise externally forced climate change is detected. If α is consistent with 1, given its uncertainty, the multi-model mean does not need to be rescaled to match the observations.

[21] We compare the regression residuals "*res*" from the observations with the samples of uncertainty "$uncertainty_i$", for both time intervals 1951–1999 and 1970–1999. For the long period we find that, in 9 out of 13 regions, the residuals lie within the range of model uncertainty. Exceptions are Central Europe (CEU), Eastern Asia (EAS), Western Asia (WAS) and the Tibetan Regions (TIB). Over the sub-period of 1970–1999, 11 out of 13 regions are within the range, with only the residuals of EAS and TIB outside the model range.

4. Results

[22] The 1951–1999 decadal global spatial trend pattern predominantly shows increases in the number of warm nights (see Figure 1a).

[23] All regional trend values of both observations and the model ensemble means are positive (see Figure 2a), however, the spread of individual model simulations do include some regional negative trends (see grey bars in Figure 2a). The spread of the model trend covers the observational trends in all regions, which underlines that the models perform reasonably well in explaining the observed values, taking into account internal variability.

[24] The sub-period 1970–1999 (Figure 2b) shows an overall increase in magnitude of the decadal trend values compared to the period 1951–1999, which agrees well

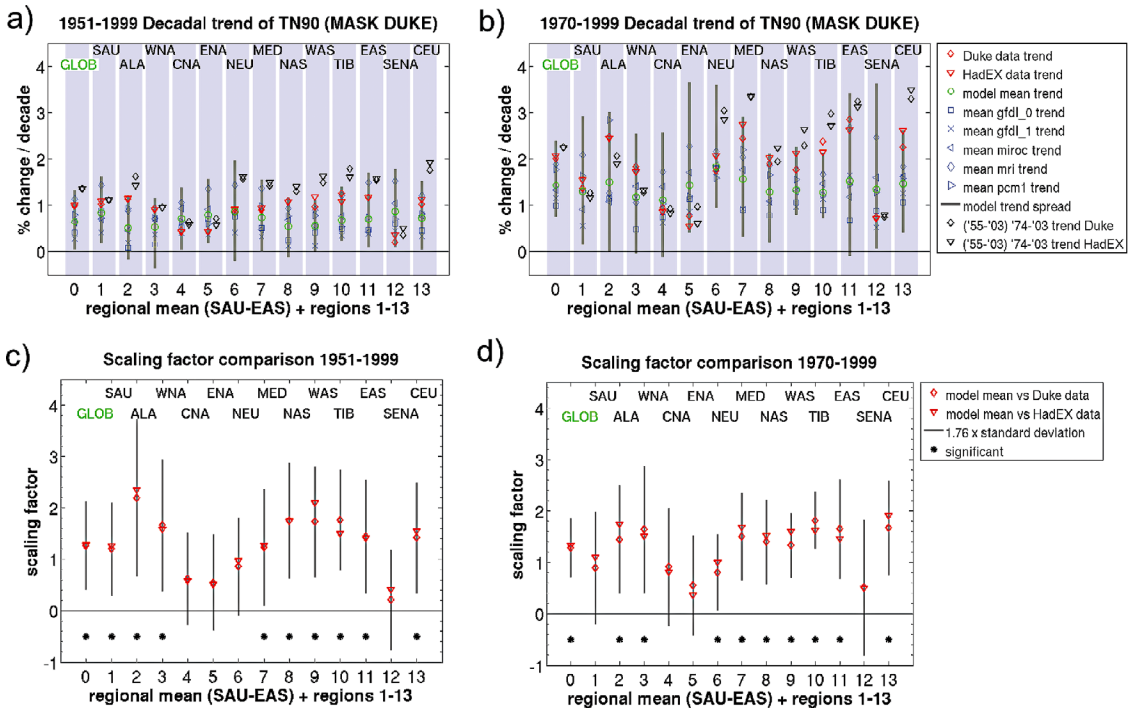

Figure 2. Spatially averaged trend of TN90 from observations (red markers) and model ensemble means (blue markers) as well as the spread of individual simulations (grey bar) for the selected regions (labelled on top and depicted against values 1–13 on x-axis) and the regional mean (labelled "GLOB", and plotted against '0' at x-axis) for the periods (a) 1951–1999 and (b) 1970–1999 (in % per decade). The black markers show results for the observed trend 1955–2003 (Figure 2a) and 1974–2003 (Figure 2b). The scaling factors (red markers) of observed changes onto the multi-model mean fingerprint for the period (c) 1951–1999 and (d) 1970–1999 are shown. Its estimated 5–95% uncertainty range is shown by the grey bar, which has been placed around the scaling factors for the Duke data. Regions with significantly detectable trend (5%) are marked by an asterisk.

between models and observations (Figures 2a and 2b). The shorter period captures the temperature increase which followed a period of stagnation of the 1950s and 1960s. This stagnation or rather reduction in extreme values of TN90 during the 1960s can be seen in all regions, in both the observed and the modelled data (see Figure 1b). This resembles changes for both observed and modeled data of the mean surface temperature.

[25] As the 20th century simulations only extend to 1999, but the observations extend at least up to 2003, we also computed observed trends over the periods 1955–2003 and 1974–2003. This allows us to assess whether more recent trends in the observed data show the same tendency as the earlier trends of 1951–1999 and 1970–1999 (see black markers Figures 2a and 2b). The results show an increase in trend for most regions, which is generally more pronounced for the 30 year period 1974–2003 (see black markers Figure 2b).

[26] Figure 2c shows the results of the fingerprint analysis. 9 out of 13 regions show a fingerprint that is significantly detectable at the 5% level, since the scaling factors of the observations are significantly larger than those from noise only, and of those 5 show a residual variability within the model range. For many regions the scaling factors are larger than one, which indicates that the observations show stronger changes than the model ensemble mean, however this difference is not significant.

[27] The results for sub-period 1970–1999 are very similar to those of the entire period (see Figure 2d). We loose the ability to detect a change in the Southern Australian (SAU) region, but now detect changes in Northern Europe (NEU) and most regions show variability within the model range. For assessing if changes in warm nights are detectable globally, we performed the regression on a vector of regional means for all 11 non-overlapping regions using area weighting and find a highly significant change both for the long and the short period (see Figures 2c and 2d, at $x = 0$, labelled "GLOB"). If the trends ending in 2003 are regressed onto the model fingerprints (for the period ending in 1999), detection results are similar.

5. Possible Causes

[28] Having found a significant externally forced increase in the number of warm nights during the second half of the 20th century, a question arises, what caused the change?

[29] Over the same period as considered here, global daily mean temperature has increased [*Trenberth et al.*, 2007], along with a rise in the number of warm days between 1951–1999 and a decrease in the diurnal temperature range (DTR) [*Vose et al.*, 2005].

[30] In order to relate these changes to each other, we investigated how monthly mean, daily mean, minimum and maximum temperature are related to the number of warm nights on inter-annual to inter-decadal timescales. Table 1, column 6, shows a tight correlation of detrended TN90 with annual mean daily mean temperatures for all regions and

global-scale data. TN90 correlates most strongly with the observed mean surface temperature, followed by the observed annual daily mean, minimum and maximum temperature (not shown). Surprisingly, the northern regions, ALA, NEU and NAS show a higher correlation of TN90 with the observed annual daily mean maximum than with the mean minimum temperature (not shown). In order to see what fraction of the significant changes in TN90 can be explained by changes in the mean surface temperature, we first regress the time series of annual mean daily mean temperature of each region on the one of TN90. Both time series have been de-trended before the regression analysis in order to base the connection on well-sampled inter-annual fluctuations only. The values of the regression coefficients are used to scale the raw time series of Tmean to determine which aspects of the changes in TN90 are explained by changes in Tmean. If the same physical connection between mean and extreme temperature operates on trend-timescales as on the shorter timescales, a large part of the trend in TN90 would be explained by the trend in mean temperature. This is found to be the case for global-scale data and many regions for both observations and model data (Figure 1b). Table 1 shows that for most regions more than half of the observed trend is explained by the observed trend in Tmean.

[31] The smoothed global-scale spatial pattern of trends in TN90 (mean subtracted) correlates, at 0.7 with that of trends in mean temperatures over the same time period (pattern not shown). This indicates that regions where mean temperatures warm stronger than the large-scale mean also tend to show stronger trends in TN90.

6. Discussion and Conclusions

[32] This study shows that the observed trends in TN90 are captured by climate model simulations. Fingerprints for the response to external forcing are detected in 9 out of 13 regions, showing that the observed trend can not be explained by internal variability alone. The residuals, unexplained variability from observations is consistent with the range of inter-model variability for most regions, which leads to a robust detection of changes globally and for SAU, ALA, WNA, MED and NAS and additionally, for the 30-year trend only, for WAS and CEU. Based on a regression of mean temperature on the number of warm nights, most of the observed trend in the number of warm nights globally, as well as for many regions, is predicted based on the trend in annual mean temperatures. *Hegerl et al.* [2007] and *Stott et al.* [2010] assessed that greenhouse gases very likely play a key role in the positive trend in the global and continental mean temperature records of the 20th century. Based on a multi-step attribution [see *Hegerl et al.*, 2010], we conclude that the global increase in the number of warm nights is probably in part due to anthropogenic influences. This may also be the case for regions with detectable changes, SAU, ALA, WNA, MED and NAS. However, as regional changes can also be affected by small-scale forcings and are more difficult to attribute to causes [see *Hegerl et al.*, 2007; *Stott et al.*, 2010], the multi-step attribution is only conclusive for global scale data.

[33] **Acknowledgments.** We would like to thank the two reviewers for their comments and suggestions, which greatly contributed to improvement of this study. Also, many thanks go to Claudia Tebaldi and Julie M. Arblaster for providing the modeled data sets of TN90. We also would like to thank Helen Hanlon for her advice. This study has been supported by the Centre for Earth System Dynamics (CESD), NFS grant ATM-0296007 and Duke University.

[34] The Editor thanks the anonymous reviewers for their assistance in evaluating this paper.

References

Alexander, L. V., et al. (2006), Global observed changes in daily climate extremes of temperature and precipitation, *J. Geophys. Res.*, *111*, D05109, doi:10.1029/2005JD006290.

Allen, M. R., and S. F. B. Tett (1999), Checking for model consistency in optimal fingerprinting, *Clim. Dyn.*, *15*, 419–434, doi:10.1007/s00382005029.

Brohan, P., J. J. Kennedy, I. Harris, S. F. B. Tett, and P. D. Jones (2006), Uncertainty estimates in regional and global observed temperature changes: A new data set from 1850, *J. Geophys. Res.*, *111*, D12106, doi:10.1029/2005JD006548.

Christidis, N., P. A. Stott, S. Brown, G. C. Hegerl, and J. Caesar (2005), Detection of changes in temperature extremes during the second half of the 20th century, *Geophys. Res. Lett.*, *32*, L20716, doi:10.1029/2005GL023885.

Giorgi, F., and R. Francisco (2000), Evaluating uncertainties in the prediction of regional climate change, *Geophys. Res. Lett.*, *27*(9), 1295–1298, doi:10.1029/1999GL011016.

Hegerl, G. C., et al. (2007), Understanding and attributing climate change, in *Climate Change* 2007*: The Physical Science Basis. Contribution of Working Group I to the Fourth Assessment Report of the Intergovernmental Panel on Climate Change*, edited by S. Solomon et al., pp. 663–745, Cambridge Univ. Press, Cambridge, U. K.

Hegerl, G. C., O. Hoegh-Guldberg, G. Casassa, M. P. Hoerling, R. S. Kovats, C. Parmesan, D. W. Pierce, and P. A. Stott (2010), Good practice guidance paper on detection and attribution related to anthropogenic climate change, in *Meeting Report of the Intergovernmental Panel on Climate Change Expert Meeting on Detection and Attribution of Anthropogenic Climate Change*, edited by T. F. Stocker et al., pp. 1–8, IPCC Work. Group I Tech. Support Unit, Univ. of Bern, Bern.

Karl, T. R., N. Nicholls, and A. Ghazi (1999), CLIVAR/GCOS/WMO workshop on indices and indicators for climate extremes: Workshop summary, *Clim. Change*, *42*, 3–7.

Karl, T. R., G. A. Meehl, T. C. Peterson, K. E. Kunkel, W. J. Gutowski Jr., and D. R. Easterling (2008), Executive summary in weather and climate extremes in a changing climate. Regions of focus: North America, Hawaii, Caribbean, and U.S. Pacific Islands, report, edited by T. R. Karl et al., U.S. Clim. Change Sci. Program and Subcomm. on Global Change Res., Washington, D. C.

Kenyon, J., and G. Hegerl (2007), Influence of modes of climate variability on global temperature extremes, *J. Clim.*, *21*, 3872–3889, doi:10.1175/2008JCLI2125.1.

Portmann, R. W., S. Solomon, and G. C. Hegerl (2009), Spatial and seasonal patterns in climate change, temperatures, and precipitation across the United States, *Proc. Natl. Acad. Sci. U. S. A.*, *106*(18), 7324–7329.

Scaife, A. A., C. K. Folland, L. V. Alexander, A. Moberg, and J. R. Knight (2008), European climate extremes and the North Atlantic Oscillation, *J. Clim.*, *21*, 72–83.

Stott, P. A. (2003), Attribution of regional-scale temperature changes to anthropogenic and natural causes, *Geophys. Res. Lett.*, *30*(14), 1728, doi:10.1029/2003GL017324.

Stott, P. A., et al. (2010), Detection and attribution of climate change: A regional perspective, *Wiley Interdiscip. Rev. Clim. Change*, *1*(2), 192–211, doi:10.1002/wcc.34.

Tebaldi, C., K. Hayhoe, J. M. Arblaster, and G. A. Meehl (2006), Going to the extremes: An intercomparison of model-simulated historical and future changes in extreme events, *Clim. Change*, *79*, 185–211.

Trenberth, K. E., et al. (2007), Observations: Surface and atmospheric climate change, in *Climate Change 2007: The Physical Science Basis. Contribution of Working Group I to the Fourth Assessment Report of the Intergovernmental Panel on Climate Change*, edited by S. Solomon et al., pp. 235–336, Cambridge Univ. Press, Cambridge, U. K.

von Storch, H., and F. W. Zwiers (2000), *Statistical Analysis in Climate Research*, Cambridge Univ. Press, Cambridge, U. K.

Vose, R. S., D. R. Easterling, and B. Gleason (2005), Maximum and minimum temperature trends for the globe: An update through 2004, *Geophys. Res. Lett.*, *32*, L23822, doi:10.1029/2005GL024379.

G. C. Hegerl and S. Morak, School of Geosciences, University of Edinburgh, West Mains Road, Edinburgh EH9 3JW, UK. (simone.morak@ed.ac.uk)

J. Kenyon, Nicholas School of the Environment and Earth Sciences, Duke University, Box 90328, Durham, NC 27708, USA.